Date of publication xxxx 00, 0000, date of current version xxxx 00, 0000.
Digital Object Identifier XX.XXXX/YYY.20XX.ZZZZZZZ

Airflow Cooling Mechanism for High Power-Density Permanent Magnet Motor

AWUNGABEH FLAVIS AKAWUNG*, (Student Member, IEEE), BESONG JOHN EBOT†, (Member, IEEE), AND YASUTAKA FUJIMOTO*†,(Senior Member, IEEE)
*Department of Mathematics, Physics, Electrical Engineering and Computer Science, Yokohama National University, Yokohama 240-0067, Japan
†Institute for Multidisciplinary Sciences, Yokohama National University, Yokohama 240-0067, Japan
Corresponding author: Awungabeh Flavis Akawung (e-mail: awungabeh-akawung-jm@ynu.jp).

ABSTRACT High-power-density electric machines present the benefits of high torque and speed. However, this generally comes with heating problems characterized by high temperatures that affect performance. Conventional approaches to address overheating are to include cooling fans or jackets within the stator core of the machine. This approach is challenging to implement in small-size high-power-density machines. In this paper, a cooling mechanism integrated in the rotor of a high-power-density permanent magnet motor is proposed. It comprises a set of six holes, shrouded within a hollow shaft. The mechanism is based on conditioning air due to a centrifugal force that is produced by the rotational speed of the rotor from the inlet. A theoretical model based on flow resistance network is proposed to analyze the airflow rate. An analytical thermal model based on lumped parameter thermal network (LPTN) is developed to analyze the effect of the flow rate on the temperature distribution in the motor. Also, a simulation analysis model was conducted using computational fluid dynamics (CFD) to analyze the effect of air flowing in the motor. An experimental prototype is developed to verify, validate, and evaluate the proposed cooling model. The cooling system is effective in reducing temperatures from speeds above 6000 min^{-1}.

INDEX TERMS Air conditioning, CFD, cooling, fan-cool, flow network, lumped parameter, mass flow, SPM motor, thermal analysis.

NOMENCLATURE

Q [L/min]	Volumetric flow rate
$\dot{m}$ [kg/s]	Mass flow rate
v, v [m/s]	Airflow velocity
A, A_D [m^2]	Area of cross-section
P_F [Pa]	Rotor pressure
F [N]	Centrifugal force
ω [min^{-1}]	Rotation speed
z [m]	Depth of ventilation duct
ρ, ρ_{air} [kg/m^3]	Density of air
k, k_{air} [W/mK]	Thermal conductivity of air
L, L_c [m]	Active and characteristic lengths respectively
R_H [Pa/ms^{-1}]	H = "in/out", "slt", and "ag" for inlet/outlet, winding slot, and air-gap flow resistances respectively
P_{in},P_{out},P_{atm} [Pa]	Inlet/outlet and atmospheric pressure respectively
q, $\dot{Q}$ [W]	Heat flux
r [m]	Radius of flow passage
R_{cond}, R_{conv}[K/W]	Thermal resistance
G_T [W/K]	Thermal conductance
R_{el} [Ω]	Phase winding resistance
i_{ac} [A]	Rated current
h [W/m^{2}K]	Heat transfer coefficient
μ [Pa.s]	Dynamic viscosity of air
H_{ag} [m]	Air-gap width
r_r [m]	Radius of rotor
L_r [m]	Length of rotor
K_f [-]	Coefficient of friction
b_r [-]	Roughness friction
N_u, R_e P_r [-]	Nusselt, Reynold, and Prandtl numbers respectively
R_{ea}, R_{er} [-]	Respective axial and radial Reynold's numbers
$\dot{Q}_{cu}$, $\dot{Q}_{mech}$ [W]	Copper and friction loss respectively

I. INTRODUCTION

There are many applications of mechatronics systems in which weight and size are the design criteria. Wearable robots are designed to be portable, mechatronics systems for agricultural purposes are designed to operate in different terrains, and industrial actuators are designed to be flexible [1]–[6]. These mechanical systems employ either pneumatic system, hydraulic system, or electric motor for actuation [2], [7]. Electric motors are desirable for construction of compact mechatronics systems because they can be optimized to meet design criteria [8]. Conversely, electric motors have relatively low output power compared to pneumatic and hydraulic actuators [9]. High output power applications that utilize electric motors employ permanent magnet (PM) motors because of their high power-density and speed [10]. Despite these merits, PM motors are faced with many challenges, the most critical of which are the losses generating heat in the motor [11]. Heating directly affects the performance and life span of the electric machine. For instance, heating facilitate wearing of winding coil insulation and causes demagnetization of permanent magnets. Power loss analysis performed in [12] reveals that the total heat generated in interior PM (IPM) motors is higher than in surface mounted PM (SPM) motors, but comparing rotor heating for both machines reveal rotors in SPM motors have higher temperatures. This can be blamed on poor heat dissipation facility in the design of high power-density SPM motors.

Depending on the application, sophisticated cooling solutions for electric motors in general, and SPM machines, have been proposed in many literature. In [13], cooling of outer-rotor SPM machine based on heat pipe is proposed. Heat is conducted through the pipes to aluminum frame heat sink. The heat absorbed by the sink is radiated to the surrounding by forced convection using external fan system. In direct fan-cooling technique of electric machines, an impeller-type fan is mounted directly at the rear end of the rotor [14]– [15]. Fan-cooling system is very efficient and is powered by the rotation of the motor and is highly influenced by the speed [16]– [17]. Also, liquid cooling techniques like cold plates and hollow conductors have been investigated for direct cooling in electric motors [18]– [19]. A major disadvantage of these techniques is the increase in size and weight of the motor to accommodate the cooling mechanism. The motor structure design must take into consideration the use of pipes, fan impellers, and liquid coolants in the case of cold plates and hollow conductors.

Much of the weight in electric machines is concentrated in the stator and rotor core. There are cooling techniques designed by structural adjustment of stator or rotor iron. In [20], a hollow rotor shaft design is investigated for cooling in SPM motors. During operation of the motor, air flows through the hollow shaft from one end to the outlet at the other end. This technique improves the rate of convection in the rotor but is disadvantageous because the thermal distance between the high loss regions of the stator assembly and the cooling air is large.

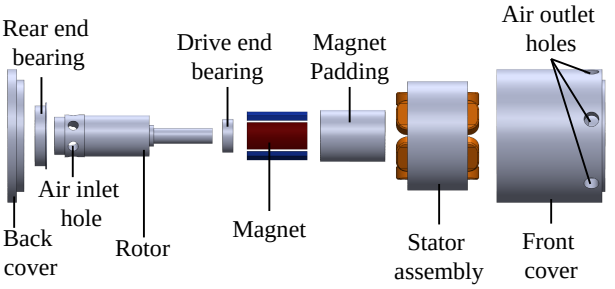

FIGURE 1: SPM motor structure with proposed airflow cooling design.

TABLE 1: Specifications of SPM Motor.

Parameter	Value	Unit
Rated speed	15000	min^{-1}
Rated torque	1.4	Nm
Rated Output power	2.0	kW
Rated current	40.0	A_{rms}
Number of slots	6	–
Number of pole-pairs	2	–
Mass	1.4	kg
Frame outer diameter	88.0	mm
Frame active length	71.0	mm
Stator outer diameter	72.0	mm
Stator inner diameter	56.0	mm
Stator stack length	40.0	mm
Air-gap	1.0	mm
Rotor outer diameter	27.0	mm
Rotor active length	46.0	mm

To solve the aforementioned problems, this paper proposes a fan-cooling mechanism based on rotor structural design. The solution employs a direct air-conditioning system which is powered by the rotation of the motor. The proposed airflow cooling SPM motor is shown in FIGURE 1. The cooling system has air inlet and outlet sections designed on the rotor and front housing respectively. The merit of the system is that no external impeller is required. The size of the machine is maintained and the weight is considerably reduced accordingly. In this research, a 2kW, 15000 min^{-1}, 3-phase SPM motor is used as experimental case study. The detail specification of the experimental SPM motor is shown in TABLE 1. The airflow cooling mechanism is evaluated in this paper.

In forced cooling of electric machines, the rate of cooling increases as the mass flux of coolant increases [21]– [22]. The mass flow rate generated in the SPM motor by the airflow cooling system is analyzed. First, the air flow field of the SPM motor without the cooling system is investigated. A comparative study is made with the air flow field analysis of the motor in presence of the cooling mechanism. The result of the comparison show that, mass flow rate of air is generated in the motor by the cooling mechanism. The term flow rate in this paper refers to the volumetric flow

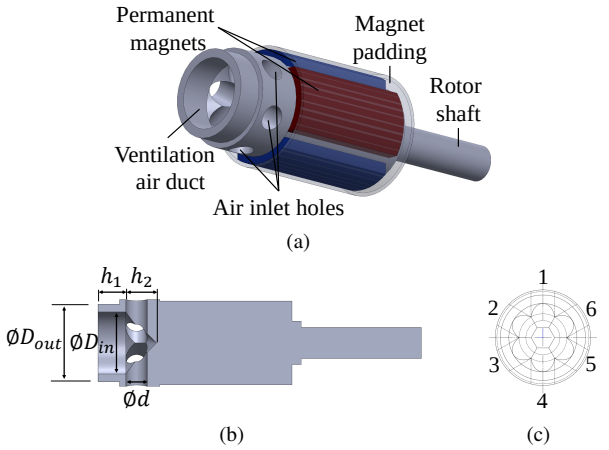

FIGURE 2: Rotor design of proposed airflow cooling mechanism (a) Rotor assembly structure (b) Section view of rotor core design (c) schematic design of ventilation duct.

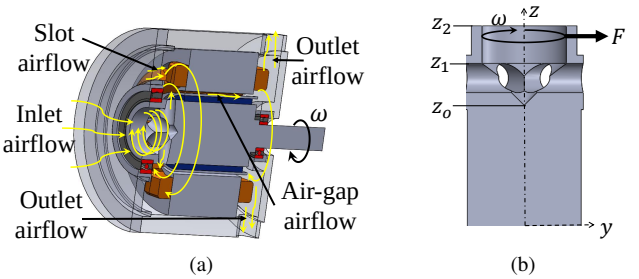

FIGURE 3: Pressure generation unit (a) Depiction of air circulation in the motor (b) Coordinate system of centrifugal acceleration.

rate except otherwise stated. Thermal analyses of the SPM motor reveal the cooling system maintains the temperature of the winding and permanent magnets within operating range during operation of the motor. The main contributions of this paper are as follows.

1) The design of a cooling system with simple cost-effective structure which is easy to implement and can achieve high cooling power at high rotational speed.
2) Also, the paper proposes an analytical model to describe the centrifugal force produced by the rotation of the rotor.
3) The implementation of an experimental prototype to verify and validate the proposed cooling system model.

The research activities in this paper are organized as follows. The geometric design considerations of the proposed cooling mechanism are discussed in Section II. A theoretical model of the air flow and temperature field of the SPM motor with the airflow cooling mechanism is developed in Section III and IV, respectively. In Section V, numerical computational fluid dynamics (CFD) simulation is performed on the CAD model of the SPM motor with and without the proposed cooling mechanism. Finally, the experimental verification of the air flow field is discussed in Section VI. In Section VII, the merits of the thermal design are clarified in comparison with selected state-of-art cooling systems.

II. AIRFLOW COOLING SYSTEM DESCRIPTION

The airflow cooling mechanism consists of air inlet section which is designed at the rear end of the rotor shaft as shown in FIGURE 2, and air outlet section which is on the front cover. The air inlet section employs a ducted fan-like system which comprises a set of six holes shrouded within a hollow cylindrical ventilation air duct as shown in FIGURE 2(a). The design considerations of the inlet holes include easiness of manufacturing by using standard drilling machines. The internal structure of the duct design is shown in FIGURE 2(b) and in this paper, the outer and inner diameters of the ventilation duct of the experimental SPM motor are given, respectively, as D_{out} = 25 mm and D_{in} = 20 mm. From a height of h_1 = 9.0 mm, the duct adopts a shallow cone-like shaped structure of depth h_2 = 10.0 mm. When in operation, accumulated air in the duct enters the motor through the set of six inlet holes each of diameter d = 7.0 mm as shown in FIGURE 2(b). The inlet holes are arranged in a circular orientation (numbered from 1 to 6 in FIGURE 2(c)) to fit the characteristics of a ducted fan propellers. During operation of the motor, a centrifugal force is produced by the rotation of the rotor. This force exerts pressure on the mass of air which accumulates in the ventilation duct. The compressed air enters the motor through the inlet holes and circulates as depicted in FIGURE 3(a). The air outlet section is a set of six holes, each of 10.0 mm diameter designed on the front cover of the motor as shown in FIGURE 1. The holes are placed towards the drive end with each hole positioned above the end-winding slot. Cooling is achieved when hot air from inside the motor flows through the outlet to the surrounding. The merit of the design is summarized as follows.

1) The mechanism is cost effective as no additional component is required. There is no need for external fan impellers as in the case of direct fan-cool systems.
2) It enable the design of compact high-power-density motors. With no external component required to implement the air conditioning system, small size electric motors can be provided with ventilation support.
3) The thermal distance between hotspots in the motor and the coolant (air in this case) is highly reduced. During motor operation, the pressure generation unit produces high turbulent flow within the motor which pushes air from the inlet duct into the motor and through all flow passages.

Initial attempts to evaluate the airflow cooling mechanism are reported in [23]–[25]. The lumped parameter thermal network model employed in these analyses did not include the node at fluid level. Also, only copper loss in the coils was considered and the flow rate was not evaluated. In this paper, the flow rate and temperature are estimated. The theoretical flow model is based on the flow network (FN) technique

presented in [25]−[26].

III. FLOW ANALYSIS

In forced cooling of electric machines, heat exchange occurs between heat generating components and the coolant. In principle, heat transfer rate in thermal systems is characterized by mass flow rate of heating and cooling mediums. The mass flow rate of coolant, having mass density ρ and flowing with velocity $\mathbf{v}$ through a surface of cross section $\mathbf{A}$ is related to the flow rate by

$$Q = \frac{\dot{m}}{\rho} = \mathbf{v} \cdot \mathbf{A} \tag{1}$$

where Q and $\dot{m}$ are the volumetric and mass flow rates of the coolant respectively. In the proposed SPM motor, the flow rate defined by (1) is due to the mechanical power of the rotor. In this paper, the computation of the flow rate is based on the descritization of (1) by using flow network technique.

A. FLOW NETWORK MODEL

As shown in FIGURE 3(b), a centrifugal force F is generated in the ventilation duct perpendicular to the axis of rotation. The force exerts a pressure P_F on the air in the duct causing it to flow along the axis of rotation into the motor as depicted in FIGURE 3(a). The pressure is computed as

$$P_F = \frac{F}{A_D} \tag{2}$$

where A_D is the area of cross section of the ventilation air duct. The force generated is proportional to the square of the motor speed, ω, and is estimated as in [25]

$$\begin{aligned} F &= \int_z (\omega^2 z) dm \\ &= \int_z (\omega^2 z) \rho_{air} dV \end{aligned} \tag{3}$$

where ρ_{air} is the density of air and the integral is computed over the volume of the ventilation duct, V, defined by the boundary $z\epsilon\,[z_0, z_2]$ indicated in FIGURE 3(b). The variation of the centrifugal force in relation to the depth of the ventilation duct and motor speed is shown in FIGURE 4. It is deduced from the graph that the force: 1) increases with increase in motor speed and 2) reduces with increase in depth of the ventilation duct, i.e., the centrifugal force is stronger at z_2 than at z_0. This characteristic of the force accounts for the change in velocity of the airflow in the duct.

The circulation of the air inside the SPM motor is constrained to hydrodynamic resistances, (or flow resistances), of the flow passages. The flow characteristic can be represented with an equivalent flow network circuit [26]−[27]. In this research, the airflow is modeled with an equivalent two channel flow network shown in FIGURE 5. The circuit constitutes the flow loops in the inlet duct, air-gap, winding slot, and the outlet. Their respective hydrodynamic resistances are denoted as R_{in}, R_{ag}, R_{slt}, and R_{out}. As reported in [26], the flow resistance unit is described by

$$\Delta P = Q^2 \cdot R_H \tag{4}$$

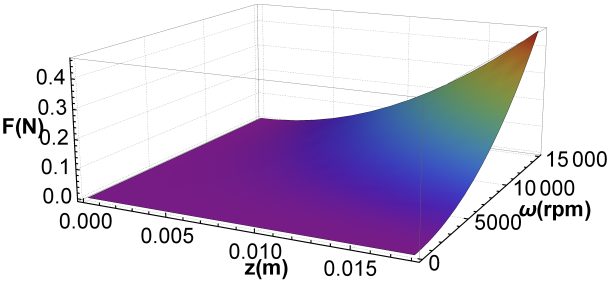

FIGURE 4: Variation of centrifugal force with depth of ventilation air duct and motor speed (assuming z_0 = 0.0 m).

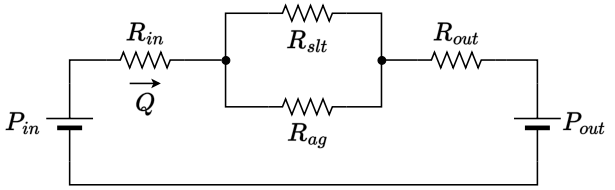

FIGURE 5: Flow resistance network of the air circulation in the proposed SPM motor.

where ΔP is the pressure difference between the inlet and outlet of the flow and R_H represents the flow resistance of the flow passage. The quadratic form of Q in (4) accounts for the turbulent nature of the flow. In purely laminar flow, Q is linear. The flow resistance is expressed as in [27]

$$R_H = \frac{8\mu}{\pi} \frac{L}{r^4} \tag{5}$$

where μ is the dynamic viscosity of air, L and r are the length and radius of the flow passage, respectively. The pressure at the inlet and outlet are denoted as P_{in} and P_{out}, respectively. The boundary conditions of the flow at the inlet and outlet is subject to constant atmospheric pressure P_{atm}. Therefore they can be expressed as

$$P_{in} = P_{atm} + P_F \tag{6}$$

and $P_{out} = P_{atm}$. The flow rate is computed by applying Ohm's law-equivalent definition expressed in (4) to the flow circuit. This gives

$$Q = \frac{z}{\sqrt{2R}} \omega \tag{7}$$

were z is the height of the ventilation duct and R is the effective flow resistance of the flow network circuit. Each flow resistance is computed by using (5). The parameters used in the computation of (7) are listed in Table 1.

IV. THERMAL ANALYSIS

To model the heat transfer process in the proposed SPM motor, thermal analysis was conducted. The objective is to determine the temperature distribution in the motor. The determination of the temperature distribution is important to properly evaluate the effect of the proposed cooling mechanism as the machine operates at different speeds.

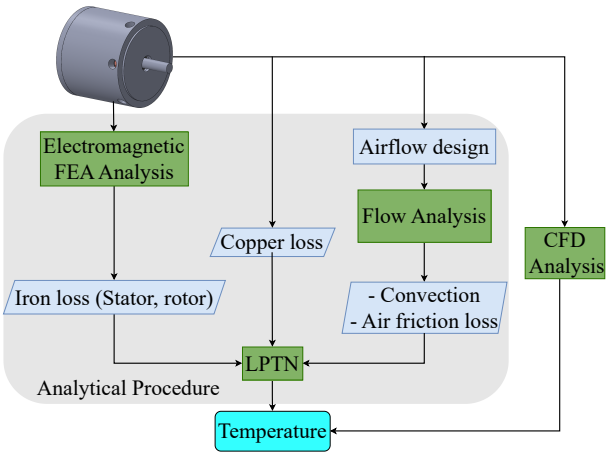

FIGURE 6: Thermal analysis procedure.

To achieve this, Lumped parameter thermal network (LPTN) technique [28]–[30] was employed. The step-by-step procedure applied in the thermal analysis is as follows.

1) Identification of thermal nodes and construction of the LPTN nework to detemine the temperature distribution in the motor.
2) Determination of the parameters of the LPTN network. This include the identification and estimation of losses in the proposed motor, determination of heat conduction thermal resistances, and modeling of heat convection.
3) Solving the network to obtain the temperature at each node.

The analysis combines the advantages of analytical and numerical thermal modeling techniques which are listed in [31]. Summarized in FIGURE 6, the losses are determined by finite element analysis (FEA) method [32] and the flow network techniques are employed in the modeling of heat convection process in the motor. Finally, CFD simulation [33] is conducted with an equivalent model of the proposed motor to determine the rate of airflow in the machine and track the temperature changes with this flow.

A. ANALYTICAL MODELING

Suppose the temperature distribution in the SPM motor is defined by T. At steady-state, the heat flux generated in the motor is absorbed by the cooling air. The heat transfer process is described by

$$k\nabla^2 T + q = hA\left(T_f - T_a\right) \tag{8}$$

where k is the effective thermal conductivity of the motor in (W/mK), q is the total loss in the motor in (W), h is the overall convective heat transfer coefficient in (W/m^{2}K), A is the area of cross section of the motor, and T_f and T_a are the temperatures of motor frame and ambient air respectively. Generally, the left-hand-side of (8) is the heat conduction in presence of heat generation sources and the right-hand-side is the convective heat transfer.

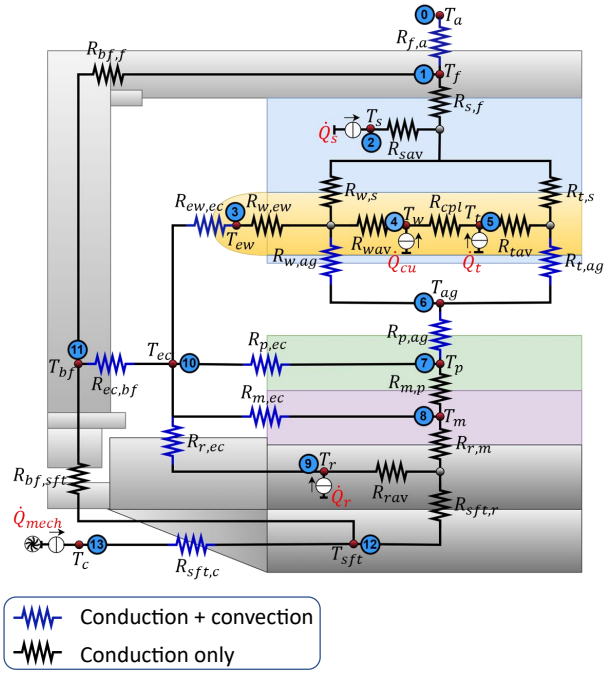

FIGURE 7: LPTN thermal network model for discretizing the heat equation of the SPM motor.

The analytical model to the heat conduction and convection problem in the SPM motor is obtained by discretizing (8) using LPTN method. To simplify the solution, the following assumptions were considered in the heat transfer process.

1) The heat transfer in the motor is due to conduction in the solid components and convection due to the airflow. Heat transfer by radiation is not considered. This is because the proposed cooling system implements forced air cooling method. As a result, the thermal resistance due to radiation is much larger than convection [34].
2) The temperature of a solid component is uniformly distributed. As a result, the radial and axial heat flow is considered in evaluating the mean temperature in the component.

The proposed LPTN is shown in FIGURE 7. The network consists of 14 temperature nodes, with each node connected to successive nodes through thermal resistances. The description of the nodes and thermal resistances are given in TABLE 2 and TABLE 3 respectively. The thermal resistances are distinguished as either conduction or convection in figure. Power loss sources in the motor are indicated as heat nodes in the LPTN. The losses in the motor are categorized and estimated in Section IV-B.

B. FEA AND LOSS ANALYSIS

To conduct the loss analysis of the proposed motor, the main power loss sources were considered. As indicated in FIGURE 7, The dominant power loss sources in the motor are due to copper loss, $\dot{Q}_{cu}$, in the winding, iron losses in the stator core, $\dot{Q}_s$, tooth, $\dot{Q}_t$, rotor, $\dot{Q}_r$, and the air friction loss, $\dot{Q}_{mech}$,

TABLE 2: Nodalization of SPM Motor.

Node	Symbol	Description
0	T_a	Mean ambient temperature
1	T_f	Mean temperature of frame
2	T_s	Mean temperature of stator yoke
3	T_{ew}	Mean temperature of end-winding
4	T_w	Mean temperature of winding
5	T_t	Mean temperature of teeth
6	T_{ag}	Air-gap air mean temperature
7	T_p	Mean temperature of padding
8	T_m	Mean temperature of magnet
9	T_r	Mean temperature of rotor iron
10	T_{ec}	End cap air mean temperature
11	T_{bf}	Mean temperature of back frame
12	T_{sft}	Mean temperature of rotor shaft
13	T_c	Mean temperature of coolant

TABLE 3: Description of Thermal Resistances in Network.

Symbol	Description
$R_{f,a}$	Frame/ambient radial thermal resistance
$R_{f,bf}$	Frame/back cover radial thermal resistance
$R_{s,f}$	Stator/frame radial thermal resistance
R_{sav}	Mean thermal resistance due to conduction in stator
$R_{w,s}$	Stator/winding/end-winding radial thermal resistance
$R_{t,s}$	Stator/tooth thermal resistance in radial direction
$R_{w,ew}$	Winding/end-winding thermal resistance
$R_{ew,ec}$	End-winding/end-cap circumferential thermal resistance
R_{wav}	Winding mean thermal resistance due to conduction
R_{cpl}	Coupling thermal resistance of axial flow in winding/tooth
R_{tav}	Mean thermal resistance due to conduction in tooth
$R_{w,ag}$	Winding/air-gap radial thermal resistance
$R_{t,ag}$	Tooth/air-gap radial thermal resistance
$R_{p,ag}$	Air-gap/padding radial thermal resistance
$R_{p,ec}$	Magnet padding/end cap air axial thermal resistance
$R_{m,p}$	Magnet/padding radial conduction thermal resistance
$R_{m,ec}$	Magnet/end cap air axial thermal resistance
$R_{r,m}$	Magnet/rotor radial conduction thermal resistance
R_{rav}	Mean thermal resistance due to conduction in rotor
$R_{r,ec}$	Rotor/end cap air axial thermal resistance
$R_{ec,bf}$	Back cover/end cap air axial thermal resistance
$R_{sft,r}$	Shaft/rotor radial conduction thermal resistance
$R_{bf,sft}$	Shaft/back cover radial conduction thermal resistance
$R_{sft,c}$	Shaft/cooling air radial conduction thermal resistance

generated by airflow dynamics in the air gap between the stator tooth and the surface of the magnet padding.

1) IRON LOSS ANALYSIS

The computation of the iron losses in the stator and rotor core are achieved through FEA analysis using *JMAG-Designer-ver19*. The procedure for conducting the analysis is illustrated in FIGURE 8. For accurate analysis, the magnetic flux distribution in the machine is determined through a magnetic field transient analysis. Upon determination of the magnetic flux distribution, loss analysis is conducted to compute the joule loss and hysteresis losses. The iron loss computation in the motor is then obtained as a summation of the joule and

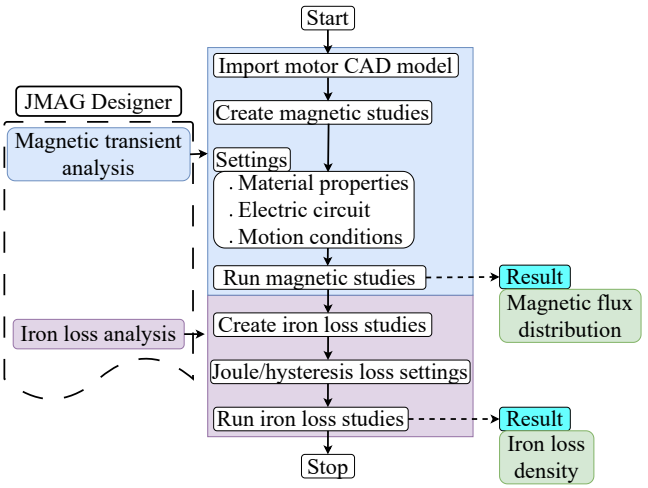

FIGURE 8: FEA Iron loss simulation procedure.

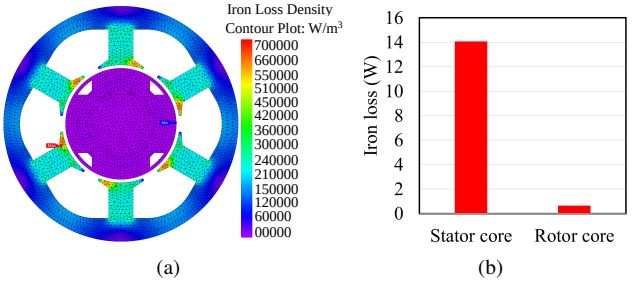

FIGURE 9: FEA iron loss calculation. (a) Iron loss density distribution (b) Iron loss results.

hysteresis losses. The iron loss density distribution is shown in FIGURE 9(a). The iron loss is maximum at the stator tooth and is above 67.5kW/m^3. This is indicated with the red arrow hotspot in the figure. The iron loss in the stator and rotor is shown in FIGURE 9(b). The iron loss in each component is the sum of the joule and hysteresis losses.

2) WINDING COPPER LOSS ANALYSIS

As already indicated above, the dominant loss source in the SPM motor is due to copper losses in the phase windings. This is as a result of joule heating from the high ac current (40 Arms) flowing in the coils. As reported in [35], the total joule loss $\dot{Q}_{cu}$ in the proposed motor due to current i_{ac} flowing in the winding is expressed as

$$\dot{Q}_{cu} = n i_{ac}^2 R_{el} \tag{9}$$

where R_{el} is the electrical resistance of the phase winding and n is the number of phases.

3) AIR FRICTION LOSS

When in operation, the air circulating in the air-gap of the motor is in direct contact with the magnet padding and the teeth of the stator. In highly turbulent flows, the air moves with high velocity and because of increase in flow rate due

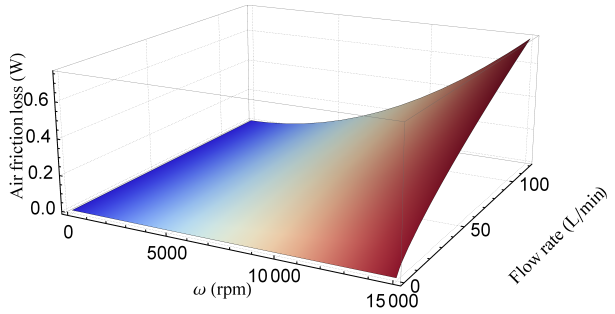

FIGURE 10: Variation of air friction loss in relation to the speed of rotation and flow rate.

to increase in speed, impact momentum increases in the air-gap. Energy is released in the form of heat in the process. A general equation for the air friction loss in the air-gap is expressed as in [35]

$$\dot{Q}_{mech} = \pi r_r^4 L_r b_r K_f \rho_{air} \omega^3 \tag{10}$$

where b_r is roughness coefficient of the component of rotor assembly in contact with the air-gap air (i.e., the magnet padding as shown in FIGURE 2(a)), K_f is the friction coefficient on the surface of the component, L_r is its axial length, and r_r is the outer radius of the rotor assembly structure. The friction coefficient is calculated as

$$K_f = \frac{0.0152}{R_{er}^{0.24}} \left[1 + \left(\frac{8}{7} \left(\frac{4R_{ea}}{R_{er}} \right) \right)^2 \right]^{0.38} \tag{11}$$

where R_{er} and R_{ea} are the Reynold's number in the radial and axial direction to the flow, respectively. The nature of the airflow is determined by the dimensionless Reynold's numbers. They can be expressed as follows.

$$R_{er} = \frac{\rho_{air}}{\mu} \omega r_r H_{ag} \tag{12}$$

and

$$R_{ea} = \frac{\rho_{air}}{\mu} L_c \cdot v. \tag{13}$$

where H_{ag} and L_c is the radial and characteristic length of the air-gap respectively, and v is the local velocity of air in the air-gap which is obtained from (1).

The variation of the air-friction loss in relation to speed of rotation and flow rate is shown in FIGURE 10. In the proposed SPM motor, the loss due to friction in the air-gap increases with increase in speed of rotation.

C. THERMAL RESISTANCE FORMULATION

The thermal resistances of the SPM motor are computed from the geometric and material properties of the motor components. The computation was performed using the correlations for determining thermal resistance of standard geometric shapes that are peculiar to electric machines [28]–[30]. For heat transfer in a metal of cross section A and length L, the thermal resistance due to conduction and convection are defined, respectively, as

$$R_{cond} = \frac{L}{kA} \tag{14}$$

and

$$R_{conv} = \frac{1}{hA}. \tag{15}$$

D. HEAT CONVECTION MODELING

Heat transfer rate by convection in the motor is determined by the heat convection coefficient h in (15). Heat convection is caused by the circulation of air in the motor. In forced convection, the air movement is due to an external force. This is achieved in this article by the centrifugal force generated by the airflow cooling mechanism. Various empirical correlations for modeling heat transfer coefficient for both forced and natural convection are studied in [36].

In general, the empirical correlation for estimating heat transfer coefficient by forced air cooling on a surface of characteristic length L_c is given as

$$h = N_u \frac{k_{air}}{L_c} \tag{16}$$

where N_u is the Nusselt number and k_{air} is the thermal conductivity of air. The Nusselt number is defined as

$$N_u = 0.023 R_e^{0.8} P_r^{0.4} \tag{17}$$

where R_e and P_r are the Reynold's and Prandtl numbers, respectively. As discussed in Section IV-B3, the nature of the flow is determined by the local velocity of the air movement on the surface. The Reynold's number is determined from the velocity as in (13). The Prandtl number accounts for the effect of natural convection component of the flow. The dimensionless constant is calculated as

$$P_r = \mu \frac{c_{air}}{k_{air}} \tag{18}$$

where c_{air} is the specific heat capacity of the cooling air.

E. TEMPERATURE COMPUTATION

Theoretical analysis of the steady-state temperature distribution in the proposed SPM motor is reported in this section. The temperature distribution is computed by solving the LPTN circuit shown in FIGURE 7. A program was written in C language to compute the thermal resistance values, and the thermal-equivalent nodal analysis technique was applied to the thermal circuit and solved using MatLab software. The temperature distribution was obtained as

$$[T] = [G_T]^{-1} \left[\dot{Q} \right] \tag{19}$$

where $[T]$, $[G_T]$, and $\left[\dot{Q} \right]$ are matrices representing the node temperatures, thermal conductance, and losses, respectively. The temperature rise at each node was calculated for different speeds of rotation. The result of the delicate parts of the stator assembly including the cover is shown in FIGURE 11. It is observed that the temperature distribution in the

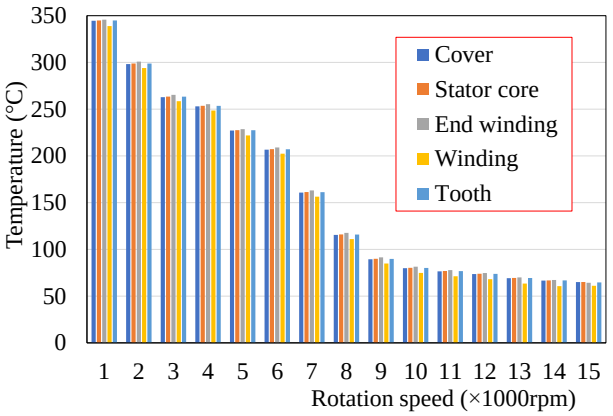

FIGURE 11: LPTN computation of the temperature rise in stator assembly and front cover of the SPM motor at different rotation speeds.

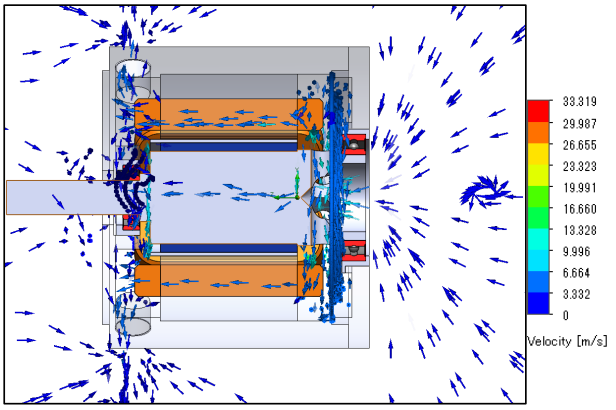

FIGURE 12: CFD analysis of the airflow vorticity in the SPM motor at 15000 min^{-1} rotation speed.

TABLE 4: Simulation Condition Settings.

Parameter	Value
Analysis type	Internal/External
Rotation speed	1000 min^{-1} to 15000 min^{-1}
Heat source	Loss sources (see Section IV-B)
Boundary conditions	
Internal analysis	Inlet/outlet pressure = 1 atm
External analysis	Motor housing = Real wall

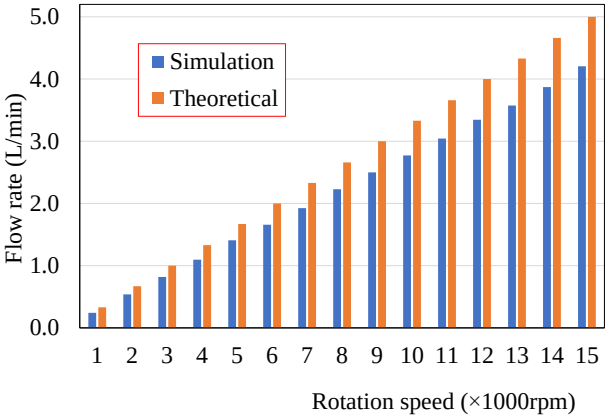

FIGURE 13: Evaluation of flow rate at a single outlet.

selected nodes reduces as speed increases which is a direct consequence of the increase in flow rate as speed increases.

V. NUMERICAL EVALUATION

In this section, the flow rate and thermal analysis models are verified by using CFD simulation. The simulation employed SOLIDWORKS flow simulation tool. To evaluate the cooling mechanism, two case studies of the SPM motor were simulated and their results were compared. The different case studies are defined as follows.

- CASE 1: SPM motor with airflow cooling system.
- CASE 2: SPM motor without airflow cooling System.

To compute the flow rate, an internal analysis type was performed on 3-D CAD model of the SPM motor in CASE 1. The configuration settings during the flow simulation studies are shown in Table 4. The external flow analysis study was performed to analyze the steady-state temperature distribution in the SPM motor of both CASE 1 and CASE 2.

A. AIR FLOW RATE COMPUTATION

The flow rates at the inlets and outlets were computed during simuation of the air flow in the SPM motor. The fluid (i.e., air in this case) volume was created in the internal analysis studies of the SPM motor in CASE 1. This was done by setting the pressure conditions of the flow at the inlet and outlet to standard atmospheric pressure. Also, the $k-\epsilon$ turbulence model was selected for the condition of the turbulence flow. To verify the analytical flow characteristic define by (7), the simulation study was configured as a parametric study in which the speed of rotation was varied from 1000 min^{-1} to 15000 min^{-1}. The result of the airflow analysis reveals two important objectives:

1) The cooling system design generates air flow in the SPM motor due to the rotation of the rotor. As shown in FIGURE 12, during operation, the air ventilation duct acts like a vortex tube. This generates high turbulence airflow in the motor.
2) The flow rate generated in the motor increases as the speed of rotation increases. Comparison of the flow rate computed at one outlet during simulation and in theoretical calculation given by (7) is shown in FIGURE 13.

At the maximum rated speed of 15000 min^{-1}, the flow rate in a single outlet is 4.2 L/min and 5.0 L/min in simulation and as predicted in theory, respectively.

B. THERMAL COMPUTATION

The thermal design objective of the SPM motor is sustainability. The motor is required to operate at normal and peak driving torque conditions while maintaining hotspot temperatures within operating range. The operating temperature

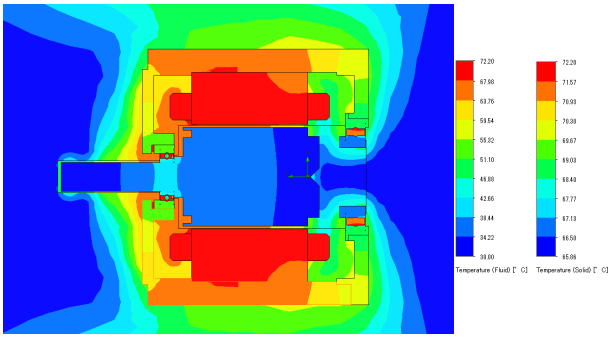

FIGURE 14: Steady-state CFD analysis of the temperature distribution in the SPM motor at 15000 min^{-1} rotation speed.

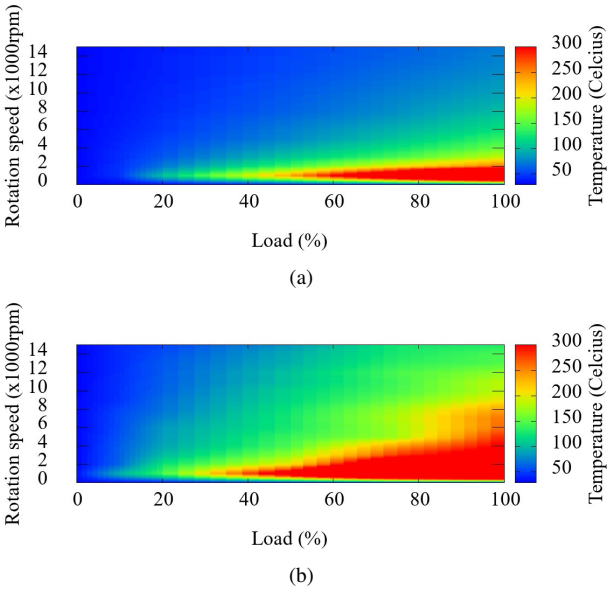

FIGURE 15: CFD analysis of temperature distribution in end winding at different speeds of rotation and load (a) steady-state analysis in CASE 1 (b) Steady-state analysis in CASE 2

range for the proposed SPM motor is 120°C. Steady-state temperature analysis of the SPM motor was performed at different load values during the CFD simulation. The contour map of the steady-state temperature distribution in CASE 1 is shown in FIGURE 14. The contour map shows simulation result at maximum rotation of 15000 min^{-1} under full load condition. It illustrates that the minimum temperature in the SPM motor is exhibited in the rotor region which is 58.32°C during full load operation. This is safe for the permanent magnets as the highest loss in the SPM motor is generated during full load operation. The map also illustrates the highest temperature in the motor is exhibited in the stator assembly region. The high temperature in this region is due to the high loss generated in the winding coils due to the current.

By comparing the temperature of the end winding computed in the simulation of the motor in CASE 1 and CASE 2, the influence of the cooling system on the temperature

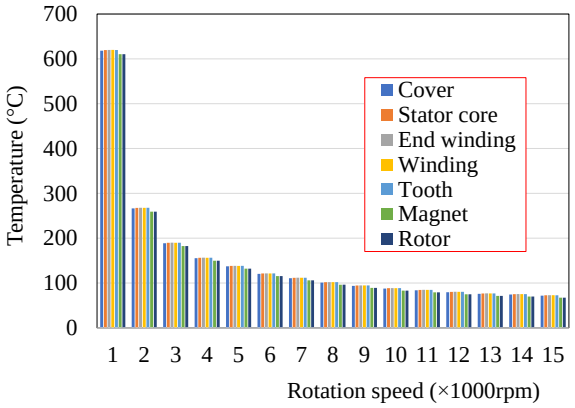

FIGURE 16: CASE 1 Steady-state full load CFD analysis result of selected nodes.

TABLE 5: Experimental Conditions.

Parameter	Value
Input voltage (V)	50
Input current(A_{rms})	$0 \sim 40$
Room temperature (°C)	25
Load torque voltage(V)	24.0
Load torque current (A)	0.12

of the motor is further clarified. This is shown in FIGURE 15. According to the contour map in CASE 1 shown in FIGURE 15(a), at speeds above 6000 min^{-1}, the motor can be operated above 50% load while maintaining the end winding temperature within operating range. For instance, at full load operation, the temperature of the end winding is 72.2°C at 15000 min^{-1} rotation speed. This is safe for the motor as it is within the operating range. The contour map in CASE 2 shown in FIGURE 15(b) clearly demonstrates the effect of the absence of the cooling system. Without the cooling system, the SPM motor cannot be operated above 20% load irrespective of the speed. At full load, the temperature of the end winding is 129.4°C at 15000 min^{-1} rotation speed. This is above the operating temperature. This comparison demonstrates that the cooling system is efficient. The temperature distribution at selected nodes in CASE 1 is shown in FIGURE 16. The result shows that the cooling system is highly influenced by the speed of rotation of the motor. This is in accordance with the prediction of the LPTN analysis shown in FIGURE 11. As the speed increases, the flow rate increases.

VI. EXPERIMENTAL VERIFICATION

To further investigate the significance of the airflow cooling system and to validate the theoretical and simulation results, a prototype SPM motor with the proposed cooling mechanism is manufactured. This is shown in FIGURE 17. The main parameters of the prototype machine are listed in Table 1. The internal structure of the prototype SPM motor is compact and is shown in FIGURE 17(a). The coils of the phase

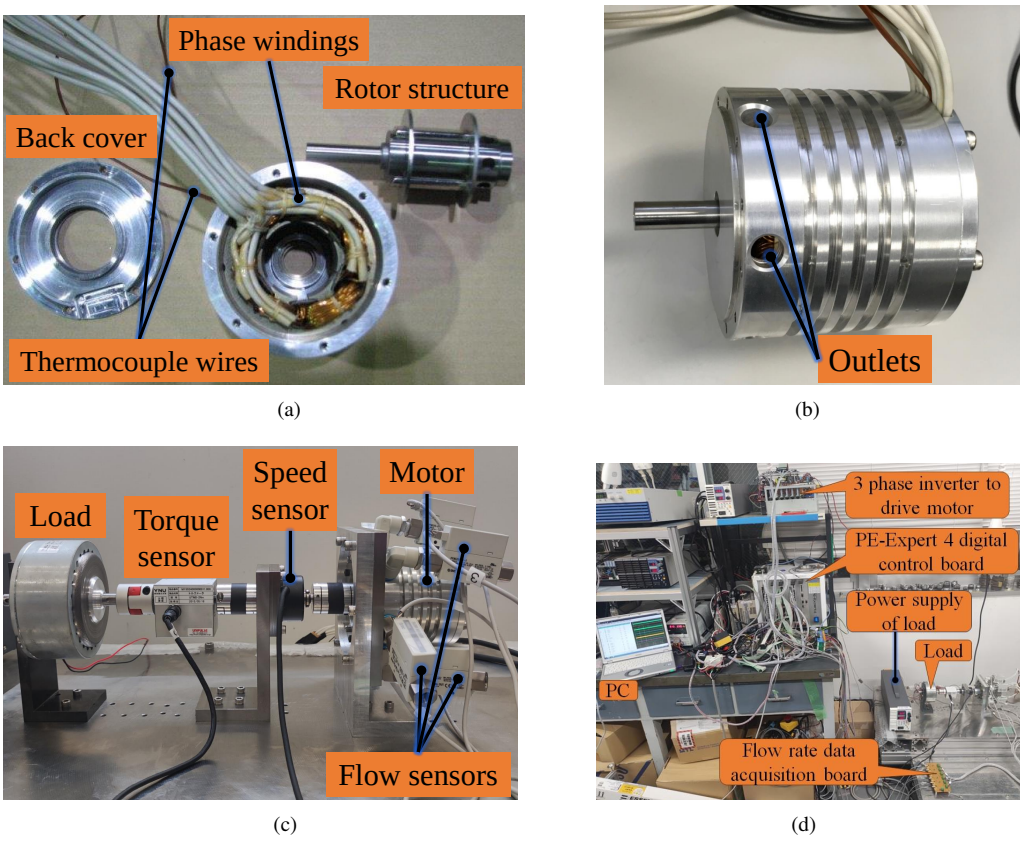

FIGURE 17: Prototype of proposed SPM motor with airflow cooling system (a) Internal structure of prototype machine (b) Coupled prototype motor showing air outlets (c) Testbench setup (d) Experimental lab setup

windings of the motor are copper-clad aluminium wire with AIW insulation type having maximum operating temperature of 220°C. The maximum operating temperature of the permanent magnets used in the prototype motor is 150°C. The high-power-density prototype motor is equipped with two K-type thermocouple wires with each connected to the end winding of two of the phase coils. During the experiment, the temperature of the end winding of the motor is monitored through the thermocouples. The complete coupling of the prototype motor with the air outlets on the cover is shown in FIGURE 17(b).

A. EXPERIMENTAL SETUP

Multiple experiments were conducted by varying the speed of rotation. An enhanced filed-oriented control (FOC) method including disturbance observer (DOB) was implemented int he experiment to control and achieve the different required speeds. This is shown in FIGURE 18. The DOB enhances the speed controller by estimating and compensating load disturbances in the experiment to satisfy speed requirements. By controlling the speed, the torque was indirectly adjusted to corresponding experimental conditions.

The MTL MEH-30-300PE rotary encoder was used as the speed sensor. The torque was constantly monitored by using the UNIPULSE UTM II 2Nm torque sensor. The experimental setup is shown in FIGURE 17(c). To measure the flow rate, an SMC PFM525 digital flow switch (±5% FS) was connected to each air outlet. The experiment was conducted under load and no load conditions. The MAGTROL HB-250 hysteresis brake was used as the load. The FOC control and data processing program were implemented in a DSP control

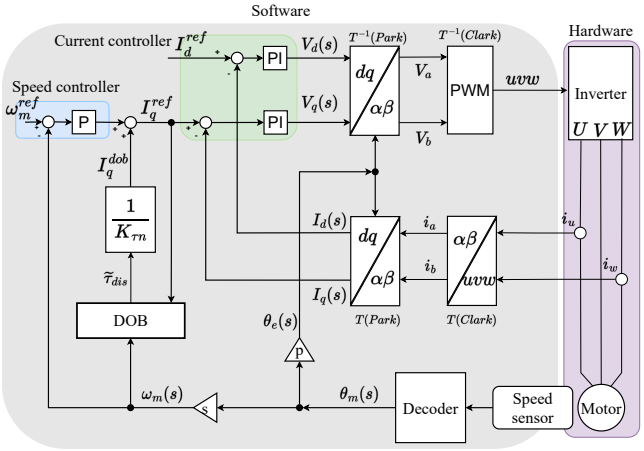

FIGURE 18: Block diagram of implementation of FOC with DOB.

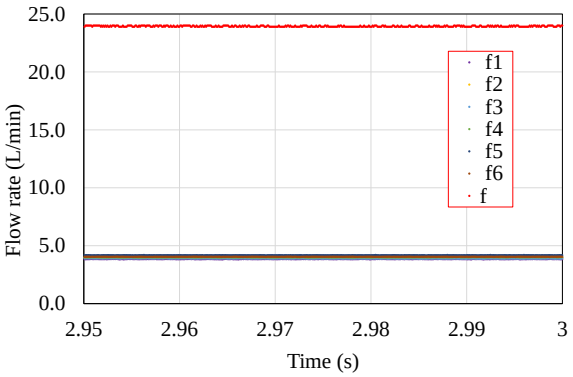

FIGURE 19: Flow rate measurement at 12000 min^{-1}.

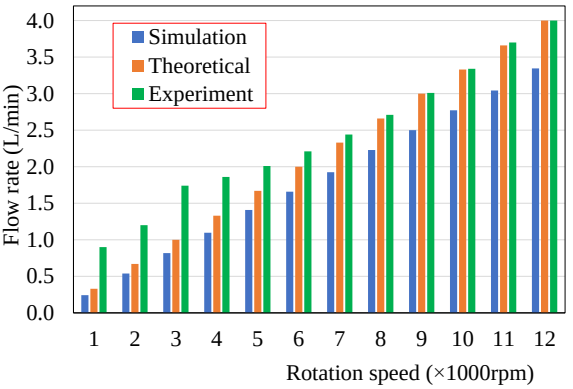

FIGURE 20: Comparison of flow rate computation method.

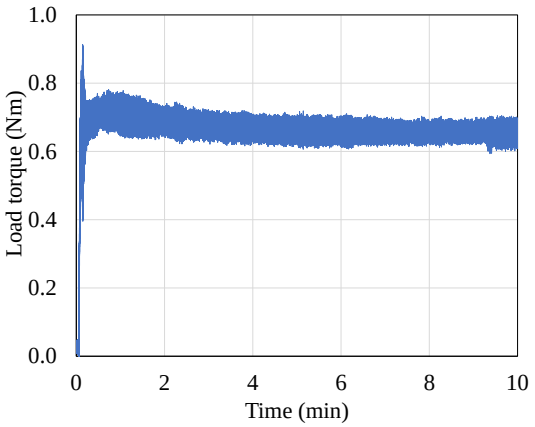

(a)

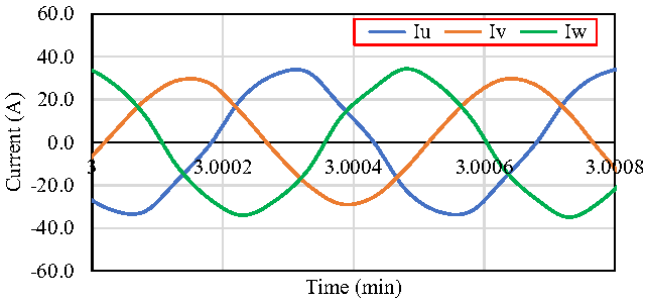

(b)

FIGURE 21: Experimental condition at 50% load (a) Load torque measurement (b) Peak-to-peak phase current.

board of MYWAY PE-EXPERT4 digital control systems. The complete experimental laboratory is shown in FIGURE 17(d). The setup comprised of data acquisition board for the flow switches and thermocouples. All data processing was performed in PE-ViewX software installed in the lab PC. The experimental conditions are shown in TABLE 5.

B. RESULT DISCUSSION

1) Flow rate measurement

The flow rate was measured at the outlets under no load condition. The experimental setup is shown in FIGURE 17(c). Measurements were taken from 1000 min^{-1} to 12000 min^{-1}. Six flow sensors were connected to the six outlets. Flow rate measurement at 12000 min^{-1} is shown in FIGURE 19. The corresponding flow rates for each outlet indicated as f1, f2, f3, f4, f5, and f6 in figure is 3.98 L/min. This result shows that the airflow design is symmetric. The total flow rate denoted by "f" in the figure is 23.88 L/min.

Comparison of the flow rates in theory, simulation, and experiment is shown in FIGURE 20. As the speed changes from 1000 min^{-1} to 12000 min^{-1}, the flow rate increases from 0.98 L/min to 3.98 L/min respectively. This illustrates that the flow rate is influenced by the speed of rotation. This tendency is similar in both the simulation and theoretical model of the proposed airflow system.

There is correlation between experimental and theoretical flow rate measurement at higher speeds. From 9000 min^{-1} to 12000 min^{-1} the flow rate measurement in both theory and experiment changes from 2.99 L/min to 3.98 L/min. However, there is discrepancy with simulation result which are lower for all speeds. This is because the measurement points for the simulation and inside the flow sensor is slightly different. In the simulation, a lid is placed at a distance which is equivalent to the length of the connection tube to the flow sensor.

2) Temperature Measurement

The flow switches were removed when conducting the temperature experiment. Based on the theoretical result shown in FIGURE 11 and evident in the simulation contour map shown in FIGURE 14, the highest temperature in the SPM motor is exhibited in the end winding. The effectiveness of the cooling system is verified by observing the end winding temperature under load condition. The thermal test was conducted at 50% load. The load was monitored by using the torque sensor and the measurement is shown in FIGURE 21(a). The peak-to-peak phase currents of the motor at 50% load recorded during the thermal test is shown in FIGURE 21(b).

Multiple experiments were conducted by changing the speed from 7000 min^{-1} to 10000 min^{-1}. Each experiment was conducted for an extended time of 600 seconds. The

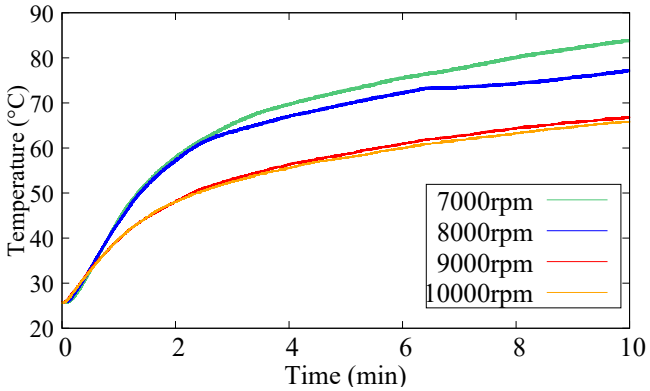

FIGURE 22: Experimental result of temperature rise in end winding at 50% load.

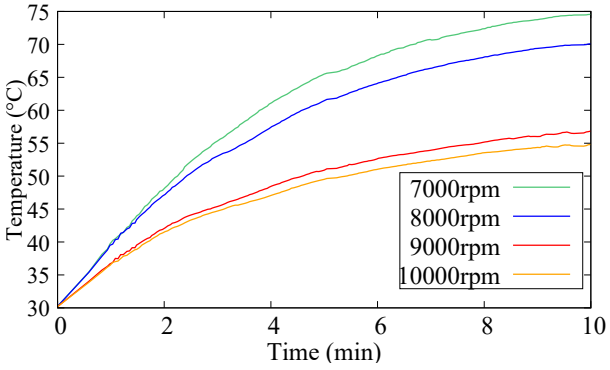

FIGURE 23: CFD analysis at 50% load of end winding of the SPM motor with the airflow mechanism.

time is long enough to get the experiment to steady state and properly evaluate the temperature of the machine. The experimental result is shown in FIGURE 22. The temperature of the machine decreases as the speed of rotation increases. This is in accordance with the CFD simulation results as is seen in FIGURE 23. Both results further confirms the prediction of the analytical LPTN model introduced in Section IV. The SPM motor benefits from the high flow rate at higher speeds due to the airflow cooling mechanism. The airflow in the motor improves the rate of convection. A Ti100 infrared thermal imager was used to monitor the temperature of the air in and out of the motor. The temperature recorded by the thermal imager at 10000 min^{-1} is shown in FIGURE 24. The room temperature is 22.9^{o}C as shown in FIGURE 24(a) and the temperature of the air coming out of the motor through the outlet is 66.2^{o}C as shown in FIGURE 24(b). This illustrates that the cooling mechanism is effective.

VII. GENERAL EVALUATION OF THE COOLING SYSTEM

A qualitative and quantitative comparative study of the proposed airflow cooling mechanism with other state-of-the-art cooling systems is shown in Table 6. In general, cooling systems are categorized as follows

1) Self-cooling techniques (SCT): Heat transfer in totally enclosed non-ventilating (TENV) systems is due to conduction in the solid components of the system. Most TENV electric motors are provided with heat sink for self-cooling of the machines.
2) Liquid cooling techniques (LCT): These employ passive vents in the motor or jackets on the motor housing which contain coolant liquids. Various fluids are used as coolants in electric machines most common of which include air, water, and oil.
3) Fan-cooling techniques (FCT): In this category, an impeller-type fan is used to blow air into the motor to increase the rate of convection.

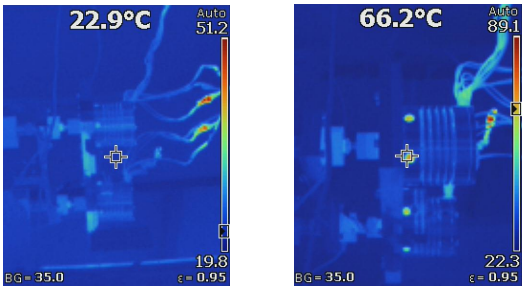

(a) (b)

FIGURE 24: Temperature of air at 10000 min^{-1} rotation speed (a) Inlet air (b) Outlet air

The choice of cooling system depends on the application of the electric machine. As shown in TABLE 6, the airflow cooling system proposed in this article is advantageous in weight-critical applications. Its implementation requires no extra components unlike the system in [13], [15], [18]–[20], and both rotor and stator cooling are achieved unlike the system in [13], [18]–[20]. Moreover, the power-density per volume of the proposed system is relatively high compared to the other systems. Also, with the exception of the system in [13], the proposed mechanism has high power-density per mass compared to other cooling systems. Also, it is observed from TABLE 6 that the proposed cooling system falls in the upper limit in terms of heat dissipation rate compared to the other cooling systems.

VIII. CONCLUSION

In order to reduce the operating temperature of SPM motors in high payload mechantronics systems, this article proposes a novel solution for cooling of small size SPM motors based on airflow. To evaluate the proposed ventilation system, a prototype SPM motor is manufactured and investigated. Theoretical, numerical, and experimental evaluation of the cooling system has been reported. This include a proof that the cooling system generates airflow in the SPM motor, estimation of the flow rate, and investigation of influence of the flow rate on the temperature of hotspots in the SPM motor.

Comparing end winding temperature in the SPM motor with/without the cooling mechanism, the effectiveness of the ventilation system is approved in simulation. This is

TABLE 6: Comparison of the Proposed Cooling Mechanism with State-of-art Cooling Systems

Reference	Cooling technique	Methodology	Max. speed (RPM)	Max. temperature (°C)	Heat dissipation rate (%)	Power density per	
						volume (kW/m^3)	mass (kW/kg)
[13]	SCT	Heat pipes and radiator	2300	86.1	27.78	(4191.7)	4.24
[15]	FCT	Impeller type fans	3600	74.1	31.39	(430.1)	0.17
[18]	LCT	Conducting plates and water pumping system	150	98.5	61.0	500*	-
[19]	LCT	Copper conductor tubes and water pumping system	3000	52.8	9.76	-	-
[20]	LCT	water pumping system	5000	26	-	6000*	0.2*
Propose method	FCT	Structural design	15000	72.6	39.5	4631.44	1.43

The values in () are calculated, while the other values are stated in the reference papers or the catalog of the machine under study.
* mean the value did not include the volume of the water pumping system and radiator size, and - means data not available or insufficient.
The power density in [13], [15] and proposed cooling mechanism include the total volume and mass of the entire cooling system.

confirmed with experimental test. The result of this research work is summarized as follows.

1) The cooling mechanism generates airflow in the motor. The pressure unit in the flow circuit was modeled theoretically. The centrifugal force generating air flow was investigated.
2) The flow rate increases with increase in speed of rotation of the SPM motor. The flow rate is investigated by using flow network technique. This is confirmed in simulation and in experiment.
3) The proposed cooling mechanism improves the rate of convection in the motor. The airflow has significant effect on the temperature of the motor. Thermal analysis of the motor is performed by LPTN, which is further verified by simulation and experiment. The result show that the temperature of the motor decreases as the speed of rotation increase.

A drawback of the proposed cooling system is that it is not effective at speeds below 5000 min^{-1}. This indicates that the system might not be suitable for low speed applications.

REFERENCES

[1] B. Noronha, C. Y. Ng, K. Little, M. Xiloyannis, C. W. K. Kuah, S. K. Wee, S. R. Kulkarni, L. Masia, K. S. G. Chua, and D. Accoto, "Soft, lightweight wearable robots to support the upper limb in activities of daily living: A feasibility study on chronic stroke patients," IEEE Trans. Neural Syst. Rehabil. Eng., vol. 30, DOI 10.1109/TNSRE.2022.3175224, pp. 1401–1411, 2022.

[2] C. T. O'Neill, N. S. Phipps, L. Cappello, S. Paganoni, and C. J. Walsh, "A soft wearable robot for the shoulder: Design, characterization, and preliminary testing," in Proc. 2017 Int. Conf. Rehabil. Robot. (ICORR), DOI 10.1109/ICORR.2017.8009488, pp. 1672–1678, 2017.

[3] A. Leu, M. Razavi, L. Langstädtler, D. Ristić-Durrant, H. Raffel, C. Schenck, A. Gräser, and B. Kuhfuss, "Robotic green asparagus selective harvesting," IEEE/ASME Trans. Mechatronics, vol. 22, DOI 10.1109/TMECH.2017.2735861, no. 6, pp. 2401–2410, 2017.

[4] H. Siebald, O. Hensel, F. Beneke, L. Merbach, C. Walther, S. M. Kirchner, and J. Huster, "Real-time acoustic monitoring of cutting blade sharpness in agricultural machinery," IEEE/ASME Trans. Mechatronics, vol. 22, DOI 10.1109/TMECH.2017.2735542, no. 6, pp. 2411–2419, 2017.

[5] E. Asadi, B. Li, and I.-M. Chen, "Pictobot: A cooperative painting robot for interior finishing of industrial developments," IEEE Robot. Autom. Mag., vol. 25, DOI 10.1109/MRA.2018.2816972, no. 2, pp. 82–94, 2018.

[6] A. Cencen, J. C. Verlinden, and J. M. P. Geraedts, "Design methodology to improve human-robot coproduction in small- and medium-sized enterprises," IEEE/ASME Trans. Mechatronics, vol. 23, DOI 10.1109/TMECH.2018.2839357, no. 3, pp. 1092–1102, 2018.

[7] W. Huo, S. Mohammed, J. C. Moreno, and Y. Amirat, "Lower limb wearable robots for assistance and rehabilitation: A state of the art," IEEE Syst. J., vol. 10, DOI 10.1109/JSYST.2014.2351491, no. 3, pp. 1068–1081, 2016.

[8] O. Beik, "Design optimization of a pm motor: A practical approach for mass production," IEEE Trans. Energy Convers., vol. 35, DOI 10.1109/TEC.2020.2991531, no. 4, pp. 1849–1858, 2020.

[9] S. Seok, A. Wang, D. Otten, and S. Kim, "Actuator design for high force proprioceptive control in fast legged locomotion," in Proc. 2012 IEEE/RSJ Int. Conf. Intell. Robots and Syst., DOI 10.1109/IROS.2012.6386252, pp. 1970–1975, 2012.

[10] T.-W. Lee, D.-K. Hong, and T.-U. Jung, "High-speed, high-power motor design for a four-legged robot actuator optimized using the weighted sum and response surface methods," CES Trans. Elect. Mach. and Syst., vol. 5, DOI 10.30941/CESTEMS.2021.00026, no. 3, pp. 224–231, 2021.

[11] S. Li, Y. Li, W. Choi, and B. Sarlioglu, "High-speed electric machines: Challenges and design considerations," IEEE Trans. Transp. Electrification, vol. 2, DOI 10.1109/TTE.2016.2523879, no. 1, pp. 2–13, 2016.

[12] N. Zhao and W. Liu, "Loss calculation and thermal analysis of surface-mounted pm motor and interior pm motor," IEEE Trans. Magn., vol. 51, DOI 10.1109/TMAG.2015.2445940, no. 11, pp. 1–4, 2015.

[13] Z. Yu, Y. Li, Y. Jing, and J. Wang, "Cooling system of outer rotor spmsm for a two-seater all-electric aircraft based on heat pipe technology," IEEE Trans. Transp. Electrification, vol. 8, DOI 10.1109/TTE.2021.3127555, no. 2, pp. 1656–1664, 2022.

[14] W. Tong, S. Wu, and R. Tang, "Totally enclosed self-circulation axial ventilation system design and thermal analysis of a 1.65-mw direct-drive pmsm," IEEE Trans. Ind. Electron., vol. 65, DOI 10.1109/TIE.2018.2823698, no. 12, pp. 9388–9398, 2018.

[15] C. Jang, J. Lee, M. Sung, and J. Lee, "Optimal design of cooling fan for 200kw class low voltage motor by numerical analysis," in Proc. 2019 IEEE Int. Electric Mach. and Drives Conf. (IEMDC), DOI 10.1109/IEMDC.2019.8785180, pp. 1163–1168, 2019.

[16] U. SanAndres, G. Almandoz, J. Poza, and G. Ugalde, "Design of cooling systems using computational fluid dynamics and analytical thermal models," IEEE Trans. Ind. Electron., vol. 61, DOI 10.1109/TIE.2013.2286081, no. 8, pp. 4383–4391, 2014.

[17] M. Roffi, F. J. T. E. Ferreira, and A. T. De Almeida, "Comparison of different cooling fan designs for electric motors," in Proc. 2017 IEEE Int. Electric Mach. and Drives Conf. (IEMDC), DOI 10.1109/IEMDC.2017.8002270, pp. 1–7, 2017.

[18] X. Fan, D. Li, R. Qu, C. Wang, and H. Fang, "Water cold plates for efficient cooling: Verified on a permanent-magnet machine with concentrated winding," IEEE Trans. Ind. Electron., vol. 67, DOI 10.1109/TIE.2019.2927181, no. 7, pp. 5325–5336, 2020.

[19] X. Chen, J. Wang, A. Griffo, and A. Spagnolo, "Thermal modeling of hollow conductors for direct cooling of electrical machines," IEEE Trans. Ind. Electron., vol. 67, DOI 10.1109/TIE.2019.2899542, no. 2, pp. 895–905, 2020.

[20] Y. Gai, M. Kimiabeigi, Y. C. Chong, J. D. Widmer, J. Goss, U. SanAndres, A. Steven, and D. A. Staton, "On the measurement and mod-

eling of the heat transfer coefficient of a hollow-shaft rotary cooling system for a traction motor," IEEE Trans. Ind. Appl., vol. 54, DOI 10.1109/TIA.2018.2860558, no. 6, pp. 5978–5987, 2018.

[21] N. Kammuang-lue, P. Sakulchangsatjatai, and P. Terdtoon, "Effect of working orientations, mass flow rates, and flow directions on thermal performance of annular thermosyphon," in Proc. 2017 8th Int. Conf. Mech. and Aerosp. Eng. (ICMAE), DOI 10.1109/ICMAE.2017.8038637, pp. 171–178, 2017.

[22] C. Liu, Z. Xu, D. Gerada, J. Li, C. Gerada, Y. C. Chong, M. Popescu, J. Goss, D. Staton, and H. Zhang, "Experimental investigation on oil spray cooling with hairpin windings," IEEE Trans. Ind. Electron., vol. 67, DOI 10.1109/TIE.2019.2942563, no. 9, pp. 7343–7353, 2020.

[23] A. F. Akawung and Y. Fujimoto, "Design and thermal analysis of cooling system for high-power density motor based on air-flow," in Proc. 2019 IEEE 28th Int. Symp. Ind. Electron. (ISIE), DOI 10.1109/ISIE.2019.8781494, pp. 273–278, 2019.

[24] A. F. Akawung and Y. Fujimoto, "Design and evaluation of airflow cooling system for high-power-density motor for robotic applications," in Proc. 2020 IEEE Energy Convers. Congress and Exposition (ECCE), DOI 10.1109/ECCE44975.2020.9236348, pp. 1715–1721, 2020.

[25] A. F. Akawung and Y. Fujimoto, "Thermal analysis of air cooling system for electric machines using lumped parameter and flow resistance network," in Proc. 2021 IEEE 30th Int. Symp. on Ind. Electron. (ISIE), DOI 10.1109/ISIE45552.2021.9576489, pp. 1–6, 2021.

[26] C. Shiyuan, "Network analyses of ventilation system for large hydrogenerator," in Proc. 2001 Fifth Int. Conf. Elect. Mach. and Syst. (ICEMS)(IEEE Cat. No.01EX501), vol. 1, DOI 10.1109/ICEMS.2001.970626, pp. 137–140 vol.1, 2001.

[27] C. Yunus, C. John, and G. Afshin, Fundamentals of Thermal-Fluid Sciences. New York, NY 10121: McGraw-Hill Education, 2012.

[28] C. Sciascera, P. Giangrande, L. Papini, C. Gerada, and M. Galea, "Analytical thermal model for fast stator winding temperature prediction," IEEE Trans. Ind. Electron., vol. 64, DOI 10.1109/TIE.2017.2682010, no. 8, pp. 6116–6126, 2017.

[29] D. Liang, Z. Q. Zhu, Y. Zhang, J. Feng, S. Guo, Y. Li, J. Wu, and A. Zhao, "A hybrid lumped-parameter and two-dimensional analytical thermal model for electrical machines," IEEE Trans. Ind. Appl., vol. 57, DOI 10.1109/TIA.2020.3029997, no. 1, pp. 246–258, 2021.

[30] J. Nerg, M. Rilla, and J. Pyrhonen, "Thermal analysis of radial-flux electrical machines with a high power density," IEEE Trans. Ind. Electron., vol. 55, DOI 10.1109/TIE.2008.927403, no. 10, pp. 3543–3554, 2008.

[31] F. Nishanth, M. Johnson, and E. L. Severson, "A review of thermal analysis and management of power dense electric machines," in Proc. 2021 IEEE Int. Electric Mach. and Drives Conf. (IEMDC), DOI 10.1109/IEMDC47953.2021.9449520, pp. 1–8, 2021.

[32] J.-Y. Ryu, S.-W. Hwang, J.-W. Chin, Y.-S. Hwang, S. W. Yoon, and M.-S. Lim, "Mathematical modeling of fast and accurate coupled electromagnetic-thermal analysis," IEEE Trans. Ind. Appl., vol. 57, DOI 10.1109/TIA.2021.3086823, no. 5, pp. 4636–4645, 2021.

[33] W. Tong, S. Wu, and R. Tang, "Research on the airflow and thermal performance in a large forced air-cooled permanent magnet synchronous machine," IEEE Access, vol. 7, DOI 10.1109/ACCESS.2019.2951919, pp. 162 343–162 352, 2019.

[34] A. Boglietti, A. Cavagnino, M. Parvis, and A. Vallan, "Evaluation of radiation thermal resistances in industrial motors," IEEE Trans. Ind. Appl., vol. 42, DOI 10.1109/TIA.2006.873655, no. 3, pp. 688–693, 2006.

[35] Q. Gao, X. Wang, Z. Deng, and Y. Zhang, "Loss calculation, analysis, and separation method of 550 000 r/min ultrahigh-speed permanent magnet motor," IEEE Trans. Ind. Electron., vol. 70, DOI 10.1109/TIE.2022.3177816, no. 4, pp. 3471–3481, 2023.

[36] D. A. Staton and A. Cavagnino, "Convection heat transfer and flow calculations suitable for electric machines thermal models," IEEE Trans. Ind. Electron., vol. 55, DOI 10.1109/TIE.2008.922604, no. 10, pp. 3509–3516, 2008.

AWUNGABEH FLAVIS AKAWUNG (Student member, IEEE) received the B.S in physics and computer science in 2009 from the University of Buea, Cameroon, the M.S in IT in 2013 through distant learning at the University of Madras in India, under the pan-African e-network project, and the M.Eng. in electrical and computer engineering in 2020 from the Yokohama National University in Japan. He is currently a Ph.D. candidate at Yokohama National University, Japan. From 2015 to 2017, he served as an assistant lecturer at the University of Buea, Cameroon. His research interests include electric machines and drives, energy conversion, motion control, and robotics.

BESONG JOHN EBOT (Member, IEEE) received the B.S., degree in physics and computer science from the University of Buea, Cameroon, in 2009 and the M.S., degree in industrial engineering from the École Nationale Supérieure Polytechnique Douala, University of Douala, Cameroon, in 2012. He received the M.E., and Ph.D., degrees in electrical and computer engineering from Yokohama National University, Yokohama, Japan, in 2018, and 2023 respectively. In summer of 2016, he conducted an research exchange program in the Department of Automation, Tsinghua University, Beijing, China.

In 2023, he joined the Typhoon Science and Technology Research Center at the Institute for Multidisciplinary Sciences of Yokohama National University as a Visiting Researcher. His research interests are in electric machines design, wireless power transfer systems, electric vehicles and new actuation technologies for mechatronics systems. Dr. Besong is a member of IEEE Magnetics Society, Industrial Electronics, Power Electronics, and Industry Applications Societies.

YASUTAKA FUJIMOTO (Senior Member, IEEE) received the B.E., M.E., and Ph.D. degrees in electrical and computer engineering from Yokohama National University, Yokohama, Japan, in 1993, 1995, and 1998, respectively. In 1998, he joined the Department of Electrical Engineering, Keio University, Yokohama, Japan. Since 1999, he has been with the Department of Electrical and Computer Engineering, Yokohama National University, where he is currently a Professor. His research interests include actuators, robotics, manufacturing automation, and motion control. Dr. Fujimoto is a Senior Member of IEE of Japan and a member of Robotics Society of Japan. He was the recipient of the IEEE/ASME Transaction on Mechatronics Best Paper Award in 2020. He is an Associate Editor for the IEEE Transactions on Industrial Electronics and a Vice Chief for the IEEJ Journal of Industry Applications.